Nanoscale Horizons

ROYAL SOCIETY OF CHEMISTRY

COMMUNICATION

View Article Online
View Journal | View Issue

Cite this: *Nanoscale Horiz.*, 2026, 11, 899

Received 14th October 2025,
Accepted 12th January 2026

DOI: 10.1039/d5nh00696a

rsc.li/nanoscale-horizons

Linear-to-circular cross-polarization differential detection for atomic co-magnetometers based on polarization-multiplexed metasurfaces

Kun Huang,[abcdef] Xu Xiao,[abcdef] Zhibo Cui,[abcdef] Liangsong Pei[abcdef] and Zhen Chai *[abcdef]

Atomic co-magnetometers, serving as high-precision magnetic field sensors, find broad applications in autonomous navigation for unmanned systems and fundamental physics. However, their conventional optical detection modules relying on bulky components suffer from limited miniaturization and integration. Metasurfaces offer a promising route toward optical path miniaturization. Nevertheless, most existing metasurface designs focus on homogeneous polarization beam splitting, such as separating linear polarization states, which can introduce additional optical noise and energy loss. To overcome this limitation, we propose a linear-to-circular polarization differential detection scheme utilizing a polarization-multiplexed metasurface. Through phase-encoded amorphous silicon meta-atoms fabricated on fused silica, this device integrates dual functional zones: a polarization-retaining deflector (PRD) and a polarization-converting deflector (PCD), enabling simultaneous beam splitting and independent manipulation of linearly polarized (LP) and circularly polarized (CP) light. At the operational wavelength of 795 nm, the meta-atoms exhibit over 80% transmittance. The PRD and PCD zones achieve deflection angles of +24.1° and −23.8°, respectively, with deviations below 1.5% from theoretical predictions. Experimental characterization demonstrates an optical rotation sensitivity of 5.9184×10^{-6} rad at 70 kHz, while the micron-scale thickness significantly enhances integration capability. This work establishes a novel paradigm for chip-scale atomic co-magnetometers and advances the convergence of nanophotonics with atomic sensing technologies.

New concepts

This represents a significant breakthrough over existing metasurface designs, which predominantly perform homogeneous polarization beam splitting (*e.g.*, separating linear polarizations). Such conventional approaches often introduce extra optical noise and energy loss. In contrast, our metasurface integrates two distinct functional zones, a polarization-retaining deflector and a polarization-converting deflector, onto a single, micron-thick chip. This allows for simultaneous beam splitting and independent manipulation of linear and circularly polarized light, a capability not achieved by prior metasurfaces. For nanotechnology and nanoscience, this work provides a new paradigm for ultra-compact, multi-functional photonic integration. It demonstrates that complex optical operations, crucial for high-precision systems like atomic sensors, can be miniaturized onto a nanophotonic platform without compromising performance, thereby advancing the convergence of nanophotonics with quantum-enabled sensing technologies.

1. Introduction

Atom co-magnetometers are high-precision magnetic measurement instruments based on atomic spin interactions.[1,2] Owing to their ultra-high sensitivity to weak magnetic fields and the advantage of not requiring a low-temperature environment, they have become crucial tools in autonomous navigation for unmanned systems,[3–5] inertial navigation,[6–8] and fundamental physics research.[9–11] Such sensors achieve magnetic measurement by accurately detecting the precession of atomic spins under the action of an external magnetic field, and the core of their performance lies in the high-precision analytical capability of the optical detection module for weak optical rotation signals. Conventional differential detection schemes predominantly rely on bulk optical components,[12] such as polarizing beam splitters (PBSs) and quarter-wave plates (QWPs), to analyze variations in orthogonally polarized linear light. While effective in suppressing source noise, the inherent millimeter-scale thickness of these components, complex optical alignment requirements, and low integration level pose significant barriers to sensor miniaturization and chip-scale implementation.

[a] *School of Instrumentation and Optoelectronic Engineering, Beihang University, Beijing, 100191, China. E-mail: zhenchai@buaa.edu.cn*
[b] *Quantum Science and Technology College, Beihang University, Beijing, 100191, China*
[c] *Institute of Large-scale Scientific Facility and Centre for Zero Magnetic Field Science, Beihang University, Beijing, 100191, China*
[d] *Hangzhou Institute of Extremely-Weak Magnetic Field Major National Science and Technology Infrastructure, Hangzhou, 370051, China*
[e] *Beihang Hangzhou Innovation Institute, Hangzhou, 310052, China*
[f] *Hefei National Laboratory, Hefei, 230088, China*

Achieving miniaturized integration of high-precision magnetometers thus necessitates overcoming the fundamental limitations of bulk optics in terms of size and integration compatibility. Recently, metasurfaces,[13–15] as a planar optical platforms composed of subwavelength structures, have demonstrated remarkable capabilities for precise manipulation of light field amplitude, phase, and polarization at the nanoscale, providing a revolutionary new approach for miniaturizing optical paths in atomic sensors. Functions such as polarization beam splitting, focusing, and modulation based on metasurfaces have been preliminarily validated in atomic magnetometers. For instance, silicon-based metasurface polarization beam splitters on sapphire substrates have achieved nanotesla-level magnetic field measurements,[16] and silicon-rich SiNx metalenses have enhanced detection efficiency in integrated systems *via* polarization multiplexing strategies.[17] Additionally, recent breakthroughs in metasurfaces have enabled more sophisticated polarization-decoupling control.[18–20] Notably, Nan *et al.* demonstrated a spatial-trajectory-based dynamic polarization manipulation strategy, where the polarization state evolves programmably along the propagation path through the strategic spatial distribution of meta-atoms. This approach establishes a novel paradigm for signal detection within intricate polarization environments.[18] The design methodology presented here draws inspiration from advances in multi-functional metasurfaces across the electromagnetic spectrum. Recent work in the terahertz regime has demonstrated how polarization-multiplexed meta-atoms can enable complex wavefront manipulation with minimal cross-talk between channels.[21] Similarly, the development of high-efficiency dielectric metasurfaces operating at terahertz frequencies has established design principles for maximizing transmittance while maintaining precise phase control.[22] These cross-spectral insights inform our approach to polarization multiplexing at optical frequencies, highlighting the transferability of nanophotonic design strategies across wavelength regimes. However, existing research primarily focuses on implementing beam-splitting functions for homogeneous polarization states[23,24] (*e.g.*, splitting linear-to-linear or circular-to-circular polarization). This single-mode splitting paradigm cannot be directly adapted to the complex optical response characteristics inherent in atomic co-magnetometers, particularly those arising from spin-exchange coupling. The inability of existing metasurface schemes to effectively compatible with such composite polarization states has become a key challenge restricting their application in differential detection of atom co-magnetometers and the realization of high-performance miniaturization. Therefore, developing novel polarization-multiplexing architectures capable of simultaneously processing both linear polarized (LP) and circular polarized (CP) light to achieve highly compatible and high-precision differential detection is a core problem urgently demanding solution in advancing the chip-scale integration of atomic co-magnetometers.

Addressing the limitations of traditional bulk optics integration and the polarization compatibility shortcomings of existing metasurface approaches, this paper proposes a novel high-precision differential detection scheme based on an innovative

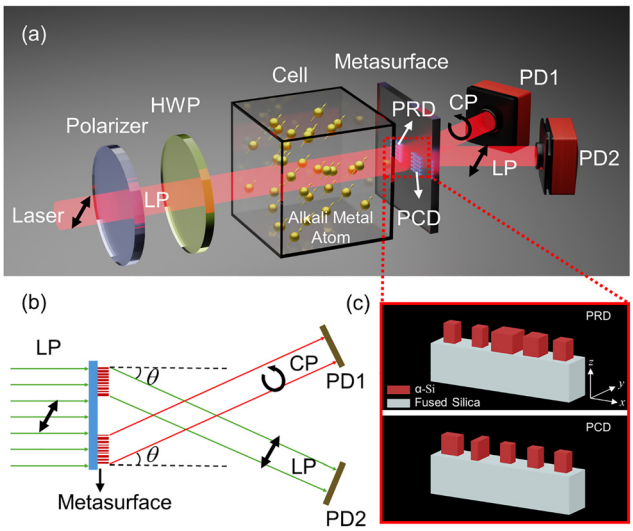

Fig. 1 Schematic of the proposed novel metasurface-enabled differential detection scheme for atomic co-magnetometers. (a) Optical layout of the linear-to-circular polarization differential detection scheme employing a polarization-multiplexing metasurface. HWP: half-wave plate; PD: photodetector; LP: linearly polarized light; CP: circularly polarized light; PRD: polarization-retaining deflector; PCD: polarization-converting deflector. (b) Illustration of the cross-deflected propagation of light beams after passing through the metasurface. (c) Unit cell configuration of the two functional regions of the metasurface, PRD and PCD, which constitute the metasurface through periodic arrangement.

polarization-multiplexing metasurface. Different from the limitation of traditional PBS that can only handle orthogonal linearly polarized light, this design realizes the synchronous beam splitting and independent regulation of linearly polarized light and circularly polarized light for the first time, perfectly matching the inherent composite polarization characteristics in the detection optical path of atom co-magnetometers. Through precise phase encoding of amorphous silicon meta-atoms on a fused silica substrate, the device integrates dual-functional regions acting as a polarization-retaining deflector (PRD) and a polarization-converting deflector (PCD), exhibiting performance superior to existing beam-splitting solutions based on liquid crystals or dielectric metasurfaces. This unique dual-channel LP/CP differential working mechanism not only significantly simplifies the optical topology but, more critically, completely circumvents the introduction of additional optical noise and energy losses associated with multiple polarization state conversions in conventional schemes.[24] Consequently, it enhances the dimensionality of information processing for the optical signal, enabling the extraction of richer atomic magnetic signal features. Experimental results demonstrate that the polarization-multiplexing metasurface device based on this scheme achieves an optical rotation angle detection sensitivity of 5.9184×10^{-6} rad at 70 kHz. Concurrently, the overall device thickness has been successfully reduced to the micrometer scale, thereby effectively addressing the inherent limitations of traditional PBSs, such as bulkiness and limited integrability.[13,15] This work not only confirms the significant potential of metasurface technology in the deep convergence of atomic precision sensing and nanophotonics, but also

establishes the proposed novel paradigm of LP/CP hybrid polarization beam splitting as a more universal approach, extendable to co-magnetometer systems incorporating various atomic species.

2. Results and discussion

2.1 Theoretical analysis of optical rotation angle detection based on polarization-multiplexed metasurfaces

Under an external magnetic field, atoms undergo polarization and exhibit spin precession. Precise measurement of the magnetic field is achieved by detecting this atomic spin precession signal. In atomic co-magnetometers, differential detection is routinely employed to enhance measurement precision and sensitivity while suppressing common-mode noise and other interferences. Currently, linearly polarized light is commonly used as the detection light, which enables precise measurement of small optical rotation angles through differential detection. When linearly polarized light passes through a vapor cell in a magnetic field, its polarization plane rotates; the magnetic field strength can be indirectly measured by detecting this rotation angle (*i.e.*, the optical rotation angle).[25–27] The working principle of optical rotation detection using LP light is grounded in light-atom interactions. According to the fundamentals of optics, an incident linearly polarized probe beam entering the vapor cell can be decomposed into left-circularly polarized (LCP, σ^+) and right-circularly polarized (RCP, σ^-) components. At the atomic level, when the atomic polarizability in the detection direction changes, the optical properties of the atoms also vary, specifically manifested as corresponding changes in the refractive indices n_+ and n_- for LCP and RCP, respectively. These changes in refractive indices depend on the number densities $\rho(-1/2)$ and $\rho(+1/2)$ in the ground state.[28]

For the D1 transition, the refractive index is given as follows:

$$n_-(\nu) = 1 + 2\rho(+1/2)\left(\frac{nr_e c^2 f_{D1}}{4\nu}\right)\mathrm{Im}(\mathcal{V}(\nu-\nu_{D1})) \quad (1)$$

$$n_+(\nu) = 1 + 2\rho(-1/2)\left(\frac{nr_e c^2 f_{D1}}{4\nu}\right)\mathrm{Im}(\mathcal{V}(\nu-\nu_{D1})) \quad (2)$$

For the atomic D2 transition, the refractive index is given analogously by:

$$n_-(\nu) = 1 + 2\left(\frac{3}{4}\rho(-1/2) + \frac{1}{4}\rho(+1/2)\right)\left(\frac{nr_e c^2 f_{D2}}{4\nu}\right)\mathrm{Im}(\mathcal{V}(\nu-\nu_{D2})) \quad (3)$$

$$n_+(\nu) = 1 + 2\left(\frac{1}{4}\rho(-1/2) + \frac{3}{4}\rho(+1/2)\right)\left(\frac{nr_e c^2 f_{D2}}{4\nu}\right)\mathrm{Im}(\mathcal{V}(\nu-\nu_{D2})) \quad (4)$$

where f_{D1} and f_{D2} denote the oscillator strengths for the D1 and D2 transitions, respectively; ν_{D1} and ν_{D2} represent the center frequencies of the D1 and D2 transitions in the alkali metal atom, both being constants; $\mathcal{V}$ denotes the Voigt profile function; and ν is the frequency of the probing light.

Following optical pumping of the atoms, we have $\rho(-1/2) \neq \rho(+1/2)$, rendering the vapor cell birefringent. Considering the detection direction aligned with the z-axis of the magnetometer coordinate system, a non-zero atomic polarization $P_z = \rho(+1/2) - \rho(-1/2)$.

After sufficient interaction between the probe light and the atoms within the vapor cell, the polarization state of the outgoing light undergoes a significant alteration. Specifically, the polarization axis of the initially linearly polarized light experiences rotation, resulting in an optical rotation angle. Research has established that a strictly proportional relationship exists between this optical rotation angle and the atomic polarization along the detection direction. This fundamental property enables us to deduce variations in the atomic polarization by precisely measuring the magnitude of the optical rotation angle. Under conditions of high-pressure broadening, the optical rotation angle θ is expressed as:

$$\theta = \frac{\pi}{2} r_e c \ln_{Rb} P_{ex}\left(-f_{D1}\mathrm{Im}(\mathcal{V}(\nu-\nu_{D1})) + \frac{1}{2}f_{D2}\mathrm{Im}(\mathcal{V}(\nu-\nu_{D2}))\right) \quad (5)$$

where P_{ex} denotes the transverse electronic polarization.

In this study, we propose a novel method of linear-to-circular polarization differential detection to address the issue of low-frequency noise. Under the balanced differential detection scheme, the light propagation process can be described using the Jones matrix formalism. Assuming the probe light is linearly polarized after passing through a polarizer from the laser output, its optical field can be represented by the following Jones matrix:

$$E = E_0\begin{pmatrix}\cos\alpha \\ \sin\alpha\end{pmatrix} \quad (6)$$

When the transmission axis of the polarizer is oriented at 45° with respect to the x-axis in the xy-plane (perpendicular to the propagation direction z), the incident linearly polarized light forms an angle $\alpha = 45°$ with the horizontal reference (*e.g.*, the x-axis), and the incident optical field can be expressed as:

$$E_{in} = \frac{\sqrt{2}}{2}E_0\begin{pmatrix}1 \\ 1\end{pmatrix} \quad (7)$$

Furthermore, the vapor cell containing alkali metal atoms can be modeled as a Faraday rotator. When the probe light traverses this cell, it experiences an optical rotation characterized by an angle θ. Consequently, the Jones matrix representing the vapor cell is given by:

$$J_{cell} = \begin{pmatrix}\cos\theta & -\sin\theta \\ \sin\theta & \cos\theta\end{pmatrix} \quad (8)$$

A horizontal polarizer with its transmission axis aligned along the x-direction is employed, which can be expressed as:

$$J_H = \begin{pmatrix}1 & 0 \\ 0 & 0\end{pmatrix} \quad (9)$$

The output light intensity after the linearly polarized light traverses the vapor cell is given by:

$$E'_{LP} = J_{cell} \cdot E_{in} = \frac{\sqrt{2}}{2} E_0 \begin{pmatrix} \cos\theta & -\sin\theta \\ \sin\theta & \cos\theta \end{pmatrix} \begin{pmatrix} 1 \\ 1 \end{pmatrix} \quad (10)$$

After passing through the polarization analyzer, the Jones matrix of the output light is:

$$E_{LP} = J_H \cdot E'_{LP} = \frac{\sqrt{2}}{2} E_0 \begin{pmatrix} \cos\theta - \sin\theta \\ 0 \end{pmatrix} \quad (11)$$

The light intensity detected by photodetector 1 is consequently:

$$I_1 = E^H_{LP} \cdot E_{LP} \quad (12)$$

When linearly polarized light is first converted to left-handed circularly polarized light (LCP) by a quarter-wave plate, then propagates through the vapor cell and horizontal polarizer, its output Jones matrix becomes:

$$E_{CP} = J_H \cdot J_{cell} \cdot J_{\lambda/4} \cdot E_{in} = \frac{\sqrt{2}}{2} E_0 \begin{pmatrix} \cos\theta - i\sin\theta \\ 0 \end{pmatrix} \quad (13)$$

The corresponding light intensity at photodetector 2 is then:

$$I_2 = E^H_{CP} \cdot E_{CP} \quad (14)$$

The expression for the optical rotation angle is obtained as:

$$\theta = \frac{1}{2} \arcsin \frac{2(I_2 - I_1)}{I_1 + I_2} \quad (15)$$

Hence, the optical rotation angle can be calculated from the intensity difference between the two photodetectors, thereby enabling the detection of optical helicity.

2.2 Design, fabrication, and characterization of polarization-multiplexed metasurfaces

Simulation and optimization were performed using the finite-difference time-domain (FDTD) method. The key structural parameters for the dielectric metasurface meta-atoms were defined as follows: nano-block height h = 500 nm, operating wavelength λ = 795 nm (corresponding to the Rb D1 line transition),[29–31] and lattice period P = 388 nm. Fig. 2a illustrates the configuration of the proposed dielectric metasurface meta-atom. It comprises a rectangular amorphous silicon (α-Si) nanopillar fabricated on a fused silica substrate. This material exhibits a high refractive index and low extinction coefficient (n = 3.746 + 0.013i) at the target wavelength, ensuring efficient optical manipulation at the subwavelength scale. Within the polarization-multiplexing metasurface, the polarization-dependent response is achieved through anisotropic rectangular meta-atoms sharing identical height and lattice periodicity. Variations in the lateral dimensions of meta-atoms locally modify the transmission and phase distribution for each independent polarization component. This control mechanism enables spatially variant phase modulation, which is precisely tailored to the specific polarization state of the incident beam.

Through numerical simulations, the transmittance (Fig. 2b) and phase (Fig. 2c) of a square lattice composed of rectangular nanopillars were obtained under illumination with linearly

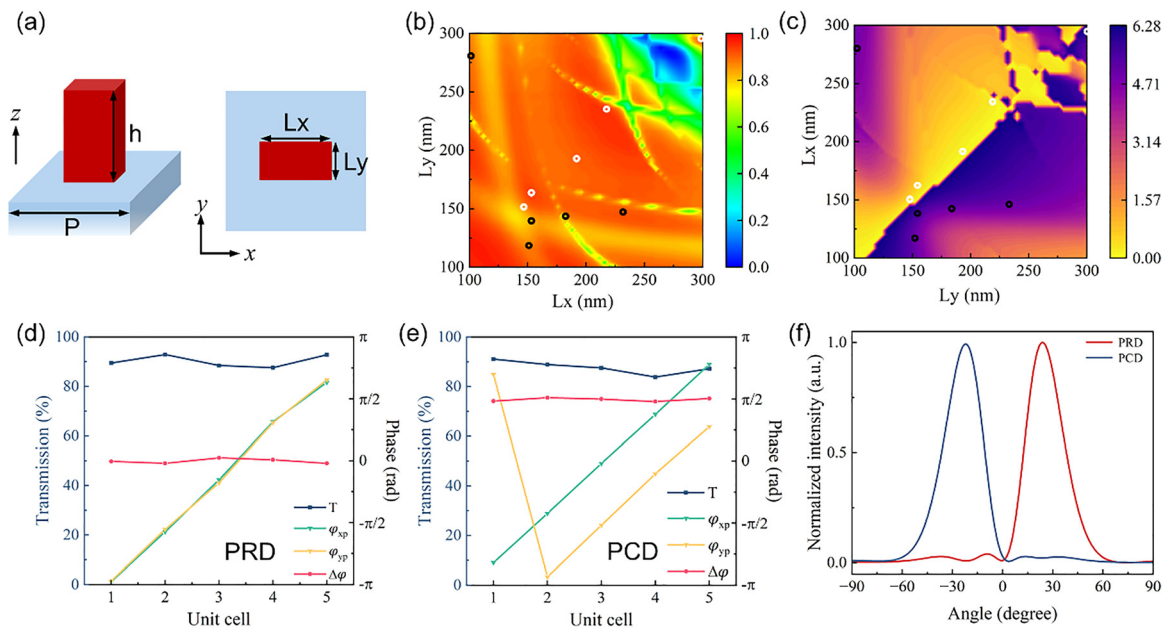

Fig. 2 Simulation results of the meta-atoms and small-scale metasurface structure. (a) Left: 3D illustration of the meta-atom with height h of 500 nm. Right: 2D illustration of the meta-atom with a lattice constant P of 388 nm. Full-wave simulations of (b) normalized transmittance and (c) phase shift for incident 45°-polarized plane waves, based on square-lattice silicon nanorod arrays with fixed lattice constant (P = 388 nm), pillar height (h = 500 nm), and swept transverse dimensions L_x and L_y. (d) and (e) Simulated transmittance and phase shift of the meta-atoms within the unit cell in (c), corresponding results for PRD and PCD marked, respectively. (f) Far-field deflection angles for incident 45°-polarized light.

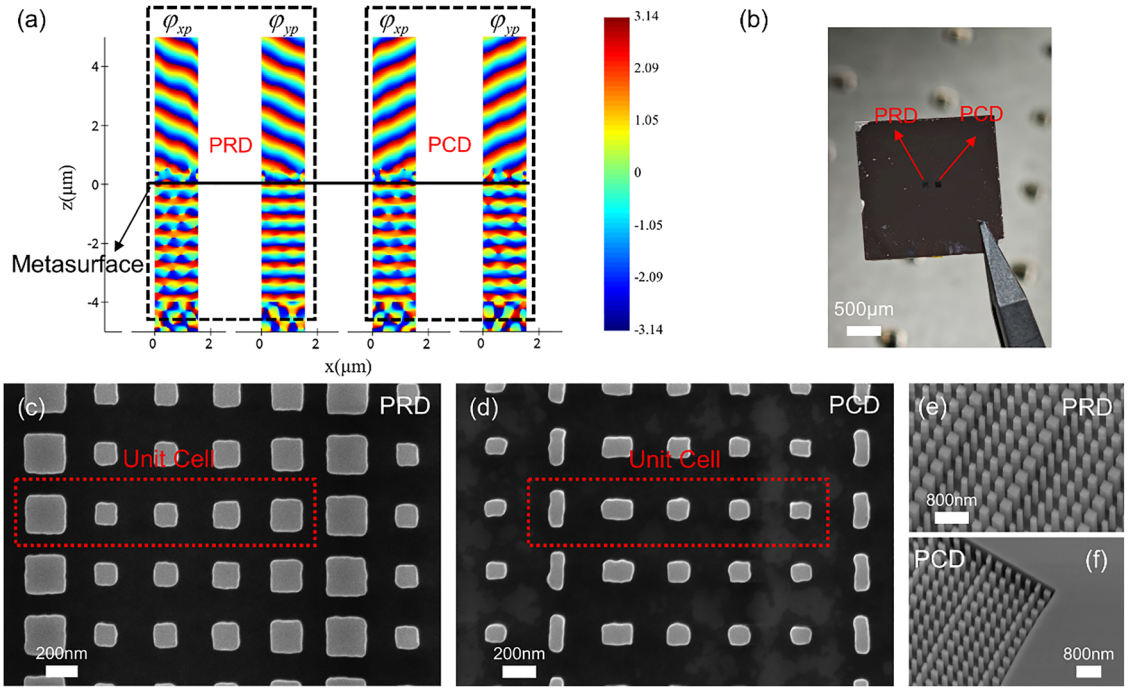

Fig. 3 (a) Spatial phase distributions transmitted through the PRD and PCD under 45° linearly polarized light incidence. (b) Optical image of the polarization-multiplexed metasurface sample. Top-down (c) and (d) and side profile (e) and (f) scanning electron microscopy (SEM) images of the fabricated polarization-multiplexed metasurface, with (c, e) and (d, f) corresponding to PRD and PCD, respectively.

polarized (LP) light oriented at 45° (p-LP light), as also detailed in SI Section I. To achieve polarization multiplexing functionality for normally incident light along the z-axis, the metasurface was partitioned into two distinct functional regions: a polarization-retaining deflector (PRD) and a polarization-converting deflector (PCD). These regions were designed to generate deflection angles of equal magnitude but opposite sign. The phase profiles for the PRD and PCD were set to $\varphi_{\mathrm{PRD}} = +\frac{2\pi}{\lambda}x\sin\theta$ and $\varphi_{\mathrm{PCD}} = -\frac{2\pi}{\lambda}x\sin\theta$, respectively. As illustrated in Fig. 1b, a deflection angle of 24.2° was selected. The metasurface construction was realized by optimizing the geometric parameters of the meta-atoms to satisfy these specified phase distributions. The design exhibits translational invariance along the *y*-direction. The fundamental unit cells for both the PRD and PCD comprise 5 meta-atoms and are periodically arranged along the *x*-direction (Fig. 1c). Fig. 2d and e depict the transmittance (>80%) of the PRD and PCD meta-atoms, alongside the corresponding polarization-resolved phase distributions obtained above the units. The red curves represent the phase difference between the *x*- and *y*-polarized components. Evidently, the phase difference for the PRD unit cell remains stable near 0, while for the PCD unit cell, it stabilizes around π/2. Furthermore, the transmission coefficients for each unit cell are plotted in Fig. S2, confirming an amplitude ratio close to unity. Additional insight into the influence of individual meta-atom structures on the polarization-multiplexed metasurface performance is provided in SI Section III. These results align with our design, demonstrating that the output light from the PRD retains linear polarization (matching the incident state), while the PCD converts the incident light into circularly polarized light. Subsequently, full-structure simulations of both the PRD and PCD regions were performed to validate the overall performance of the polarization-multiplexed metasurface device. Fig. 3a displays the distribution of the transmitted phase under p-LP illumination, clearly showing beam deflection at an angle θ. Among them, the phase distributions in the two directions simulated for PRD are basically the same, *i.e.*, the phase delay is essentially zero. This indicates that the transmitted light is converted into LP light. Similarly, the phase distributions in the two directions simulated for PCD differ by π/2, indicating that the transmitted light is CP light. Fig. 2f presents the deflection angles and normalized energy distributions for the PRD and PCD in their respective target directions. The simulated deflection angles are +24.1° and −23.8°, respectively. According to the generalized Snell's law[32,33] ($\theta = \arcsin(\lambda/N_{\mathrm{p}})$, where N is the number of meta-atoms per unit cell), the theoretically predicted deflection angle is $\theta = \pm 24.2°$. The simulation results exhibit excellent agreement with the theoretical calculations, with deviations less than 1.5%. In addition, we conducted simulations to characterize the far-field electric field profiles and polarization states for both the PRD and PCD regions. Quantitative analysis *via* far-field integration reveals that the energy proportions for the two channels are ∼85% and ∼83%, resulting in a power distribution ratio of approximately 1.02 : 1. These results confirm that a well-balanced optical power distribution is realized between the two detection channels (Fig. S4). Collectively, these simulation results confirm the successful design of a high-efficiency polarization-multiplexing metasurface.

Our fabrication process employed electron-beam lithography (EBL) to pattern the metasurface, followed by silicon layer etching using a chromium (Cr) hard mask, as schematically illustrated in Fig. S5 (see Methods section for details). Fig. 3b illustrates the fabricated polarization-multiplexing metasurface sample. The functional regions, corresponding to the PRD and PCD sections, each feature a footprint of 800 μm × 800 μm with a center-to-center spacing of 1 mm. Additionally, to prevent interference from transmitted light through the non-functional regions, a continuous layer of amorphous silicon (α-Si) thin film was deposited across these areas. This design effectively suppresses additional optical crosstalk caused by stray light during the detection process. Scanning electron microscopy (SEM) images of the fabricated polarization-multiplexing metasurface are presented in Fig. 3c–f. Analysis of the fabricated sample revealed two primary deviations from the ideal structure: (1) the silicon etch depth was approximately 10 nm less than the target value, and (2) individual meta-atoms exhibited slightly tapered sidewall profiles, with an estimated taper angle of 5° ± 1°. These effects are attributed to anisotropic etching behavior and etch rate drift, likely caused by charge accumulation at the amorphous silicon (α-Si)/fused silica substrate interface.[16] Fig. S6–S8 provide a detailed quantitative analysis of the fabrication defects in the samples arising from the micro-nanofabrication process.

2.3 Optical characterization

Following the fabrication of the polarization-multiplexing metasurface, its optical performance was characterized experimentally. The measurement setup is illustrated in Fig. 4a. Metasurface properties were probed using a 795 nm distributed Bragg reflector (DBR) laser under near-normal incidence. To ensure linear polarization with variable orientation, the laser light was first linearly polarized by a polarizer, and its polarization angle (ψ = 45°) was set by rotating a subsequent half-wave plate. The sample was mounted on a rotational three-axis translation stage. Precise alignment was optimized to achieve uniform transmission for the two beams generated by

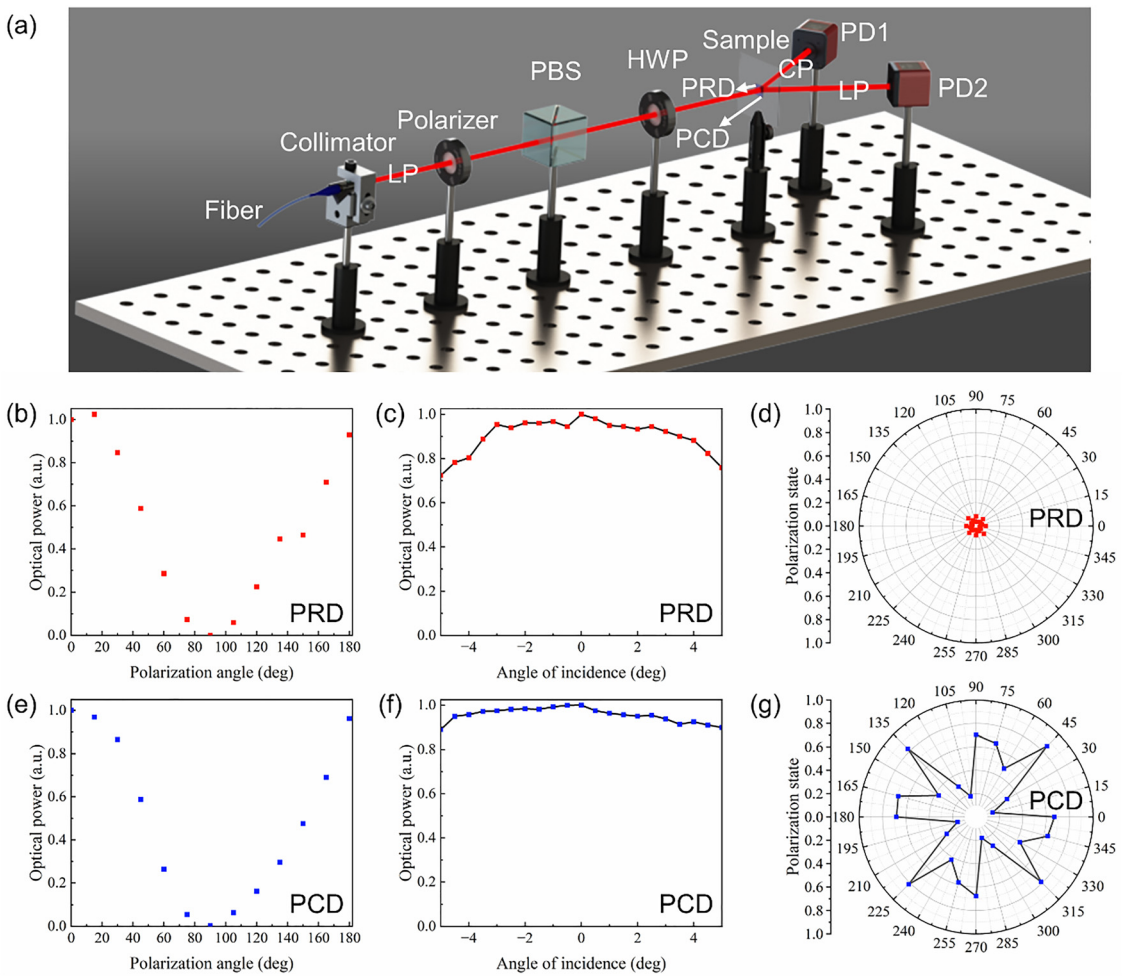

Fig. 4 Experimental characterization of the optical properties of the polarization-multiplexed metasurface. (a) Experimental setup for testing the optical properties of the fabricated metasurface. (b)–(d) and (e–g) correspond to the PRD and PCD functional regions, respectively. (b) and (e) Normalized optical power in the far-field *versus* polarization angle of incident linearly polarized (LP) light. (c) and (f) Normalized transmitted optical power as a function of incident angle. (d) and (g) Quantitative relationship between output polarization state and incident LP polarization angle, where polarization state values of 0 and 1 represent LP and circularly polarized (CP) light, respectively.

the metasurface. As designed, the PRD and PCD functional regions of the metasurface split the incident 45° linearly polarized beam into two separate paths. These beams propagate at distinct angles to ensure effective spatial separation. Specifically, the beam transmitted through the PRD region retains its original linear polarization, while the beam from the PCD region is converted into circular polarization. Fig. 4b and e demonstrate that the transmitted light intensity through each region follows a cosine-squared dependence on the incident polarization angle. This behavior strictly adheres to Malus's law, characteristic of a linear polarizer.[34] To characterize the sensitivity of the polarization-multiplexing metasurface for detecting optical rotation angles, we further evaluated the PRD and PCD performance, focusing on the normalized optical power and the polarization state of the transmitted light under varying incident angles. These parameters directly influence the fundamental optical properties of the metasurface and consequently determine the sensitivity and accuracy of the detection system. Misalignment between the probe beam, vapor cell, and metasurface axis can induce transmission deviations, critically impacting the signal-to-noise ratio. Therefore, we analyzed the normalized optical power over an incident angle range of −5° to +5° (Fig. 4c and f). The results indicate that the normalized power remains within an acceptable range for both PRD and PCD. Even under the most extreme condition (incident angle = −5° for PRD), the transmitted power exceeds 70% of its value at normal incidence, demonstrating the metasurface's strong resilience to incident angle variations. Nevertheless, precise axial alignment between the incident light, vapor cell, and metasurface must be ensured during routine operation. This investigation confirms the stability of the detection sensitivity for the atomic co-magnetometer under practical alignment tolerances. Furthermore, by varying the polarization angle of the incident LP light, we characterized the polarization state of the output beams from the PRD and PCD. Fig. 4d and g show the evolution of the output polarization states. At the design polarization angle (ψ = 45°), the output states align with our design specifications: linear polarization for the PRD beam and circular polarization for the PCD beam. We also examined the polarization state dependence on the incident angle for different input polarization angles; the results show consistent behavior compared to normal incidence (Fig. S9). Additionally, the diffraction efficiency for different orders under varying input polarization angles was investigated (Fig. S10). The results confirm that the transmitted energy from the PRD is predominantly concentrated in the +1st diffraction order, while the PCD output is concentrated in the −1st order, consistent with the design. The relatively low diffraction efficiency observed in the target order likely stems from the discrete phase sampling of the meta-atoms. In future work, adopting continuous-shaped metasurface architectures could effectively suppress background stray light and minimize phase abruptness, thereby significantly improving the overall diffraction efficiency.[19]

The beam quality of the transmitted light was monitored using a beam profiler (BC207VIS/M). Representative beam profiles for the PRD and PCD outputs are presented in Fig. 5a and b, respectively. To verify the deflection angles, a small-diameter (1 mm) probe beam was successively incident on the PRD and PCD regions, and the propagation of the output beams was tracked. As shown in Fig. 5c and d, the beam spot position was recorded at intervals of 0.1 mm along the

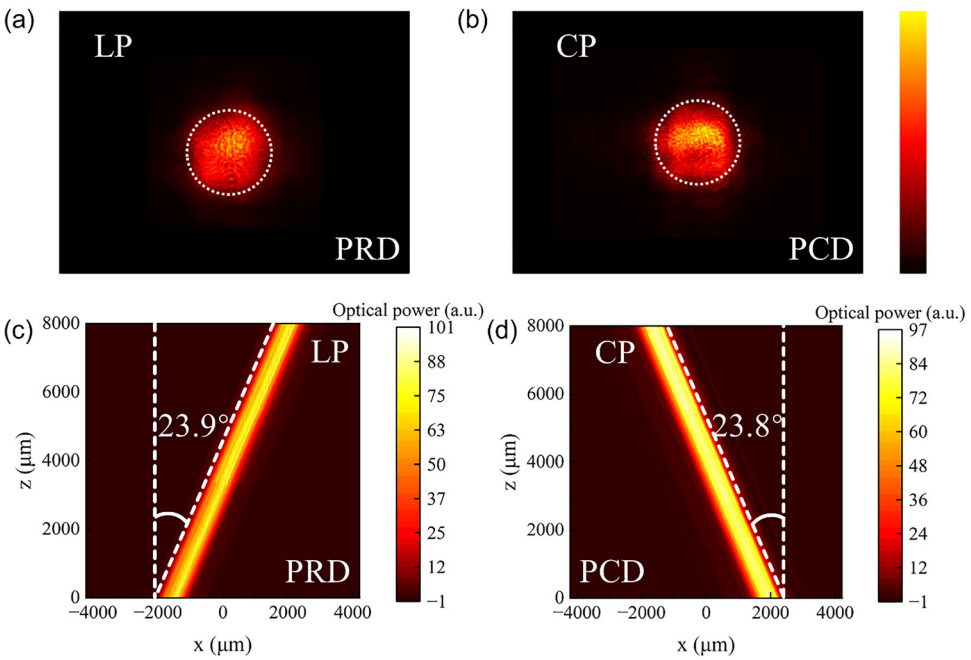

Fig. 5 Performance characterization of the polarization-multiplexed metasurface. (a) and (b) Diffraction patterns of incident light transmitted through the PRD and PCD, respectively. (c) and (d) Beam propagation diagrams for diffracted light passing through the PRD and PCD, respectively.

propagation direction (z-axis) using the three-axis stage. Stitching 80 images revealed the distinct propagation paths and confirmed the deflection effect. The experimental results demonstrate that our polarization-multiplexing metasurface successfully generates the corresponding LP and CP beams from the PRD and PCD regions, respectively, deflected at the designed angles. Crucially, the mutually converging deflection paths of the two beams are advantageous for reducing the integrated volume with the photodetectors. This characteristic provides an essential experimental foundation for the further integration of miniature atomic comagnetometers.

2.4 Optical rotation angle detection and sensitivity

The sensitivity of the optical rotation angle signal was measured using the fabricated polarization-multiplexing metasurface device. As depicted in Fig. 6a, the experimental setup is schematically illustrated; details regarding the connections between the actual optical path and the signal detection module are available in Fig. S11. A probe beam generated by a DBR laser was delivered *via* polarization-maintaining fiber and collimated using an appropriate collimator to match the sample size. To simulate minute optical rotation angles for sensitivity testing, a terbium gallium garnet (TGG) magneto-optic crystal (Verdet constant = 60 rad T^{-1} m^{-1}@795 nm) replaced the alkali vapor cell. The Faraday effect induces a rotation of the linear polarization plane when light propagates parallel to an applied magnetic field. The rotation angle θ is given by $\theta = VBL$, where V is the Verdet constant, B is the magnetic flux density, and L is the crystal length. A 20-mm-long TGG crystal was housed inside a cylindrical magnetic shield (permalloy) to attenuate ambient fields. An external AC magnetic field was generated by a 120-turn solenoid coil driven by a sinusoidal current at 70 kHz from a function generator (Keysight 33500B). When the laser traversed the crystal within the magnetic field, the Faraday effect induced by the axial field variation produced an optical rotation angle θ. This rotation signal was detected and demodulated using a low-noise current amplifier (SRS 570) and a lock-in amplifier (MFLI, Zurich Instruments). Finally, the system yielded a photocurrent signal directly proportional to the rotation angle.

The differential amplified signal was demodulated using the 70 kHz reference signal. The demodulated output underwent low-pass filtering with a cutoff frequency of 100 Hz. The amplitude of the output signal was measured under varying drive current amplitudes. Fig. 6b shows the system output voltage responding to the AC current amplitude, effectively generating signals proportional to minute rotation angles. Linear regression analysis of the data yields $\Delta V = 0.06405\Delta I$, indicating a strong linear correlation. When the drive current is increased by 100 mA, there is an effective polarization rotation of 4.55×10^{-4} rad and a 6.405 mV increase in the output signal. This scaling relationship links the spectral

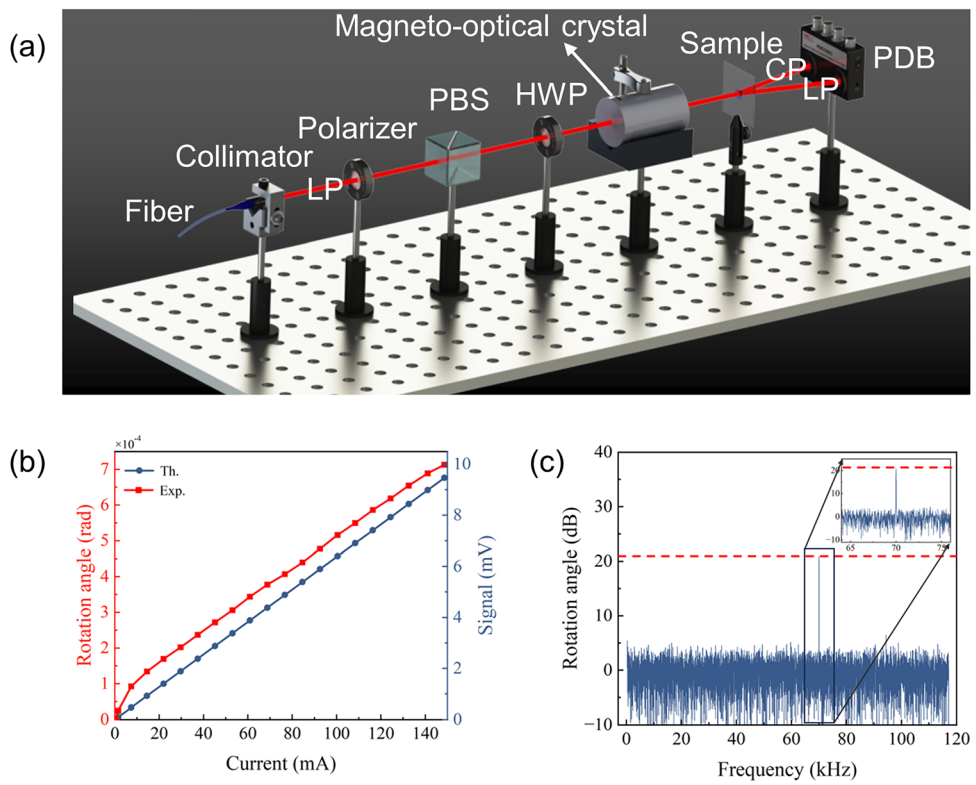

Fig. 6 Resolution characterization of optical rotation angle *via* differential detection using polarization-multiplexed metasurfaces. (a) Experimental setup for angular resolution measurement using the metasurface. PDB: balanced photodetector. (b) Theoretical optical rotation angle and the measured output signal *versus* coil drive current. (c) Measurement of optical rotation angle sensitivity achieved with the polarization-multiplexed metasurface. The inset shows the sensitivity around 70 kHz.

signal, output voltage, and optical rotation angle, as illustrated in Fig. 6c. Under steady-state conditions, the noise voltage at the lock-in amplifier output was approximately 7.384 μV. Comparing this noise level to the signal amplitude change per radian allows calculation of the minimum resolvable rotate on angle. Additionally, we utilized Power Spectral Density (PSD) to analyze the signal components and quantify the signal amplitude at the 70 kHz operating frequency (see Fig. S12). Analysis shows the system achieves a minimum measurable rotation angle of 5.9184×10^{-6} rad (corresponding to the noise voltage), demonstrating impressive angular measurement sensitivity. In atomic sensors, the optical rotation angle depends on the applied magnetic field, probe wavelength, vapor pressure within the cell, and operating temperature. Detection typically requires resolving minimum rotation angles on the order of $\approx 10^{-6}$ to 10^{-8} rad.[24,35] Consequently, this polarization-multiplexed metasurface can be employed for the detection of optical rotation angles in conventional atomic comagnetometers.

3. Conclusion

In summary, we propose a novel high-precision differential detection scheme based on a polarization-multiplexing metasurface, addressing the critical limitations of bulky optics and limited integration in atomic sensor detection modules. Fabricated by patterning amorphous silicon (α-Si) on a fused silica substrate according to phase distributions derived from the generalized Snell's law, the device comprises two functional regions: the polarization-retaining deflector (PRD) and the polarization-converting deflector (PCD). A meta-atom database exhibiting transmittance exceeding 80% at the target operational wavelength of 795 nm was established through simulation-driven design. Subsequent rigorous optical characterization *via* simulations confirmed that the PRD and PCD deflect incident light at +24.1° and −23.8°, respectively, while simultaneously generating linearly polarized (LP) and circularly polarized (CP) output states. These results demonstrate excellent agreement with theoretical predictions, exhibiting deviations of less than 1.5% in deflection angle and matching the designed polarization states. Furthermore, the device exhibits robust angular tolerance; even under the most extreme incident angle condition (−5° on the PRD), the transmittance remains above 70% of its normal-incidence value. Experimental validation of the metasurface's sensitivity for optical rotation angle detection achieved a remarkable angular sensitivity of 5.9184×10^{-6} rad@70 kHz. This performance overcomes the inherent constraints of conventional polarization beam splitters (PBS), namely their large volume and integration challenges. Moreover, as the polarization-multiplexing metasurface is fabricated from dielectric materials, it is compatible with on-chip silicon-on-insulator (SOI) processes. This compatibility holds promise for the future development of metasurface-based atomic sensors featuring ultra-high sensitivity, compact size, and high portability.

4. Methods

4.1. Metasurface fabrication

Fabrication of polarization-multiplexed metasurfaces was performed on 500-μm-thick fused silica substrates. Initially, the substrates underwent standard cleaning procedures, followed by deposition of a 500-nm-thick amorphous silicon (α-Si) layer *via* plasma-enhanced chemical vapor deposition (PECVD). A positive-tone electron beam resist (ARP6200.09) was then spin-coated onto the α-Si film. Electron beam lithography (EBL) was conducted at 4 nA beam current with a dosage of 325 μC cm^{-2} to pattern the metasurface design. Post-EBL development, a 50-nm chromium (Cr) hard mask was deposited at 4 nm min^{-1} using a high-vacuum evaporation system. Lift-off processing was subsequently carried out in *N*-methyl-2-pyrrolidinone (NMP) solvent to remove residual resist. Pattern transfer to the α-Si layer was achieved through inductively coupled plasma reactive ion etching (ICP-RIE) using C_4F_8/SF_6 gas chemistry, selectively removing unmasked α-Si regions. Finally, the samples were immersed in a chromium etchant solution to strip remaining Cr residues.

Conflicts of interest

There are no conflicts to declare.

Data availability

The data supporting this article have been included as part of the supplementary information (SI). Supplementary information is available. See DOI: https://doi.org/10.1039/d5nh00696a.

Acknowledgements

This research was supported by General Program of Zhejiang Provincial Natural Science Foundation of China (LZ24F050007), National Natural Science Foundation of China (62373028), Beijing Natural Science Foundation (4232071).

References

1 D. Budker and M. Romalis, Optical magnetometry, *Nat. Phys.*, 2007, **3**, 227–234.
2 J. Kitching, *et al.*, Atomic sensors – A review, *IEEE Sens. J.*, 2011, **11**, 1749–1758.
3 M. Barczyk and A. F. Lynch, Integration of a triaxial magnetometer into a helicopter UAV GPS-Aided INS, *IEEE Tran. Aerosp. Electron. Syst.*, 2012, **48**, 2947–2960.
4 A. Manzanilla, *et al.*, Autonomous navigation for unmanned underwater vehicles: Real-time experiments using computer vision, *IEEE Robot. Autom. Lett.*, 2019, **4**, 1351–1356.
5 L. Xue, *et al.*, Integrated attitude estimate algorithm for INS/Magnetometer system based on data fusion of dual MIMU inertial array, *IEEE Sens. J.*, 2025, **25**, 25410–25419.
6 A. Canciani and J. Raquet, Absolute positioning using the earth's magnetic anomaly field, *Navigation*, 2016, **63**, 111–126.

7 M. Kok, *et al.* presented in part at MEMS-based inertial navigation based on a magnetic field map, Vancouver, Canada, 2013.
8 Z. T. Wu, *et al.*, An experimental evaluation of autonomous underwater vehicle localization on geomagnetic map, *Appl. Phys. Lett.*, 2013, **103**, 104102.
9 A. Ajoy, *et al.*, Atomic-scale nuclear spin imaging using quantum-assisted sensors in diamond, *Phys. Rev. X*, 2015, **5**, 011001.
10 A. Canciani and J. Raquet, Airborne magnetic anomaly navigation, *IEEE Tran. Aerosp. Electron. Syst.*, 2017, **53**, 67–80.
11 D. M. Jackson, *et al.*, Quantum sensing of a coherent single spin excitation in a nuclear ensemble, *Nat. Phys.*, 2021, **17**, 585–590.
12 L. H. C. Patterson, *et al.*, Balanced polarimeter: A cost-effective approach for measuring the polarization of light, *Am. J. Phys.*, 2014, **83**, 91–94.
13 Y. Ozeki, *et al.*, Quantum-enhanced balanced detection for ultrasensitive transmission measurement, *J. Opt. Soc. Am. B*, 2020, **37**, 3288–3295.
14 L. Stern, *et al.*, Chip-scale atomic diffractive optical elements, *Nat. Commun.*, 2019, **10**, 3156.
15 J. J. Zhang, *et al.*, Ultra-compact, efficient and high-polarization-extinction-ratio polarization beam splitters based on photonic anisotropic metamaterials, *Opt. Express*, 2022, **30**, 538–549.
16 X. T. Yang, *et al.*, Atomic magnetometry using a metasurface polarizing beamsplitter in silicon-on-sapphire, *ACS Photonics*, 2024, **11**, 3644–3651.
17 J. S. Hu, *et al.*, Integrated optical rotation detection scheme for chip-scale atomic magnetometer empowered by silicon-rich SiNx metalens, *Opt. Lett.*, 2024, **49**, 3364–3367.
18 T. Nan, *et al.*, Generation of structured light beams with polarization variation along arbitrary spatial trajectories using tri-layer metasurfaces, *Opto-Electron. Sci.*, 2024, **3**, 230052.
19 M. Pu, *et al.*, Catenary optics for achromatic generation of perfect optical angular momentum, *Sci. Adv.*, 2015, **1**, 1500396.
20 S. Sun, *et al.*, Polarization-Improved Bidirectional-Pump Atomic Magnetometer Based on Spin-Decoupled Metasurface, *Adv. Sci.*, 2025, **12**, 09028.
21 W. Xu, *et al.*, Polarization-multiplexing metasurfaces for tunable wavefront configurations via Moiré engineering, *Photonics Res.*, 2025, **13**, 2130.
22 H. Li, *et al.*, Spin-dependent amplitude and phase modulation with multifold interferences via single-layer diatomic all-silicon metasurfaces, *Opto-Electron. Sci.*, 2025, **4**, 240025.
23 Z. B. Cui, *et al.*, Ultra-compact and high-precision differential detection method based on liquid crystal polarization grating for miniature atomic magnetometer, *Nanophotonics*, 2024, **13**, 4255–4265.
24 Y. Xu, *et al.*, Atomic spin detection method based on spin-selective beam-splitting metasurface, *Adv. Opt. Mater.*, 2024, **12**, 2301353.
25 C. Johnson, *et al.*, Magnetoencephalography with a two-color pump-probe, fiber-coupled atomic magnetometer, *Appl. Phys. Lett.*, 2010, **97**, 243703.
26 S. P. Krzyzewski, *et al.*, Characterization of noise sources in a microfabricated single-beam zero-field optically-pumped magnetometer, *J. Appl. Phys.*, 2019, **126**, 044504.
27 V. Shah and M. V. Romalis, Spin-exchange relaxation-free magnetometry using elliptically polarized light, *Phys. Rev. A: At., Mol., Opt. Phys.*, 2009, **80**, 013416.
28 S. J. Seltzer, PhD thesis, Princeton University, 2008.
29 Y. Chen, *et al.*, Spin exchange broadening of magnetic resonance lines in a high-sensitivity rotating K-Rb-21Ne co-magnetometer, *Sci. Rep.*, 2016, **6**, 36547.
30 R. Mottola, *et al.*, An efficient, tunable, and robust source of narrow-band photon pairs at the 87Rb D1 line, *Opt. Express*, 2020, **28**, 3159–3170.
31 Q. Q. Yu, *et al.*, Partial measurements of the total field gradient and the field-gradient tensor using an atomic magnetic gradiometer, *Phys. Rev. A*, 2023, **107**, 043110.
32 F. Aieta, *et al.*, Aberration-free ultrathin flat lenses and axicons at telecom wavelengths based on plasmonic metasurfaces, *Nano Lett.*, 2012, **12**, 4932–4936.
33 N. F. Yu, *et al.*, Light propagation with phase discontinuities: Generalized laws of reflection and refraction, *Science*, 2011, **334**, 333–337.
34 X. T. Yang, *et al.*, Analysis of atomic magnetometry using metasurface optics for balanced polarimetry, *Opt. Express*, 2023, **31**, 13436–13446.
35 S. Li, *et al.*, Optical rotation in excess of 100 rad generated by Rb vapor in a multipass cell, *Phys. Rev. A: At., Mol., Opt. Phys.*, 2011, **84**, 061403.

